Highly Conductive Titanium Oxynitride Electron-Selective Contact for Efficient Photovoltaic Devices

Xinbo Yang, Yuanbao Lin, Jiang Liu, Wenzhu Liu, Qunyu Bi, Xin Song, Jingxuan Kang, Fuzong Xu, Lujia Xu, Mohamed N. Hedhili, Derya Baran, Xiaohong Zhang, Thomas D. Anthopoulos, Stefaan De Wolf*

Prof. Dr. Xinbo Yang
College of Energy, Soochow Institute for Energy and Materials InnovationS (SIEMIS), Soochow University, Suzhou 215006, PR China
E-mail: louis.yang@gmail.com

Dr. Xinbo Yang, Mr. Yuanbao Lin, Dr. Jiang Liu, Dr. Qunyu Bi, Dr. Xin Song, Mr. Jingxuan Kang, Mr. Fuzong Xu, Dr. Lujia Xu, Prof. Dr. Derya Baran, Prof. Dr. Thomas D. Anthopoulos, Prof. Dr. Stefaan De Wolf
KAUST Solar Center, King Abdullah University of Science and Technology (KAUST), Thuwal 23955-6900, Saudi Arabia
E-mail: xinbo.yang@kaust.edu.sa; stefaan.dewolf@kaust.edu.sa

Dr. Wenzhu Liu
Research Center for New Energy Technology, Shanghai Institute of Microsystem and Information Technology (SIMIT), Chinese Academy of Sciences, Jiading, 201800 Shanghai, PR China

Prof. Dr. Xiaohong Zhang
Institute of Functional Nano & Soft Materials (FUNSOM), Jiangsu Key Laboratory for Carbon-Based Functional Materials & Devices, Collaborative Innovation Center of Suzhou Nano Science & Technology, Soochow University, 199 Ren'ai Road, Suzhou, 215123, Jiangsu, PR China
E-mail: xiaohong_zhang@suda.edu.cn

Dr. Mohamed N. Hedhili
KAUST Core Lab, King Abdullah University of Science and Technology (KAUST), Thuwal 23955-6900, Saudi Arabia.

Abstract: High quality carrier-selective contacts with suitable electronic properties are a prerequisite for high power conversion efficiency (PCE) photovoltaic devices. In this work, an efficient electron-selective contact, titanium oxynitride (TiO_xN_y), is developed for crystalline silicon (c-Si) and organic photovoltaic devices. Atomic-layer deposited TiO_xN_y is demonstrated to be highly conductive with a proper work function (4.3 eV) and a wide band gap (3.4 eV). Thin

TiO_xN_y films simultaneously provide a moderate surface passivation and enable a low contact resistivity on c-Si surfaces. By implementation of an optimal TiO_xN_y-based contact, a state-of-the-art PCE of 22.3% is achieved on a c-Si solar cell featuring a full-area dopant-free electron-selective contact. Simultaneously, conductive TiO_xN_y is proven to be an efficient electron-transport layer for organic photovoltaic (OPV) devices. A remarkably high PCE of 17.02% is achieved for an OPV device with an electron transport TiO_xN_y layer, which is superior to conventional ZnO-based devices with a PCE of 16.10%. Atomic-layer deposited TiO_xN_y ETL on a large area with a high uniformity may help accelerate the commercialization of emerging solar technologies.

Photovoltaic (PV) technology, which converts inexhaustible solar energy into electricity, offers an economic and sustainable solution to the challenge of increasing energy demand in times of global warming. The world PV market is currently dominated by wafer-based crystalline silicon (c-Si) PV technology, occupying a very high market share of ~95% in 2019,[1] thanks to its combination of high power conversion efficiency (PCE), long stability, use of non-toxic and abundant materials, as well as its well-developed, scaled processing techniques. By the end of 2018, the accumulated PV capacity worldwide reached > 500 GW, generating ~ 0.28% of the world's commercial electricity consumption.[1,2] Commercial c-Si PV modules, featuring an average PCE of 17-20%, exhibit a high reliability with limited PCE degradation over their guaranteed period, typically 25 years, resulting in an average energy payback time of only ~ 2 years in Europe.[1]

Currently, the main objective of c-Si PV technology development is to increase the PCE and reduce further the production costs, aiming to reduce the levelized cost of electricity (LCOE). The PCE of conventional c-Si solar cells based on diffused p-n junction is significantly limited by the high carrier recombination velocity at the metal-silicon contact regions. When directly in contact

with c-Si, metals induce large densities of electronic states near the interface within the bandgap of silicon, resulting in >50% recombination losses in high efficiency c-Si solar cells.[2] In addition, heavily doping also induces Auger recombination, bandgap narrowing and free carrier absorption in c-Si, which further limit the device performance.[3] Recent years have seen the successful development of advanced passivating-contact technology,[3-5] boosting the PCE of c-Si solar cells over 26%.[6-7] High-quality passivating contacts reduce the carrier recombination effectively at both contact and non-contact regions, and selectively extract one type of charge carrier (*e.g.*, the holes), while blocking the opposite type (*e.g.*, the electrons). In the meantime, passivating contacts also offer a suitably low contact resistivity (ρ_c) and enable one-dimensional carrier extraction, reducing resistive losses. The most successful passivating contact technologies are based on doped silicon layers, specifically, silicon heterojunction technology (SHJ) and polycrystalline silicon on oxide contacts (POLO, also referred to as tunnel oxide passivating contact, TOPCon).[6-7] However, both SHJ and POLO structures suffer from optical losses due to the parasitic absorption of silicon layers, and deposition process involves toxic and flammable gases (*e.g.*, silane, phosphine) with mandatory safety control. Dopant-free passivating contacts based on wide bandgap materials (*e.g.*, metal oxides, metal nitrides, alkali metal fluorides),[8-16] which were deposited by thermal evaporation, atomic layer deposition (ALD) or magnetic sputtering, have been developed to overcome the drawbacks. With high transparent electron-selective TiO_2 and hole-selective MoO_x contacts, c-Si solar cells with the best PCEs of 22.1% and 23.5% have been achieved, respectively, employing a simple full-area contact architecture.[8,12] It is widely-accepted that c-Si solar cells with passivating contacts on both polarities will be the inevitable next step for the mainstream PV industry.

Meanwhile, the PV community is in search of alternatives to single-junction c-Si PV technology, either to boost further the performance of c-Si solar cells, such as tandem solar cells, or for niche applications, such as building-integrated photovoltaics (BIPV). To this end, organic solar cells are emerging as a promising PV technology, thanks to its simple device structures, low-cost solution-processing, light-weight, flexibility and transparency.[17,18] In the past decade, the PCE of single-junction organic photovoltaic (OPV) devices has been significantly improved from ~5% to a current value of >17%, [19,20] and tandem OPV devices reach PCEs as high as 17.3%,[21] demonstrating the high competitiveness of OPVs among the next-generation, high-performance low-cost PV technologies.

Typically, the OPV device architecture, as well as c-Si solar cells with passivating contacts, features a sandwich structure, consisting of transparent conductive oxide (TCO), electron-transport layer (ETL), the absorber, hole-transport layer (HTL) and metal electrodes. The carrier transport layers play a critical role in achieving high performance and stable PV devices by featuring adequate electrical properties (*e.g.*, work function, conductivity, band alignment). Therefore, important efforts have been devoted to the development of new interfacial materials, particularly ETLs such as ZnO,[22] TiO$_2$,[23] poly[9,9-bis(6′-bromohexyl)fluorene-alt-co-1,4-phenylene (PFN-Br),[24] PDINO[25] *etc*. Among these, the transition metal oxides (*e.g.* TiO$_2$ and ZnO) have also been developed as dopant-free passivating contacts for c-Si solar cells.[3,4,8,10] To date, TiO$_2$ and ZnO have already been demonstrated to be universal and efficient ETLs for different PV technologies, owing to their suitable electronic properties and ease of deposition. However, TiO$_2$ and ZnO deposited by either ALD or solution processing exhibit a low conductivity, and thermal annealing (typically 100 - 500°C) or elemental doping is usually required to achieve a low contact resistivity for PV devices. Therefore, a highly-conductive, stable ETL with a suitable band

alignment to the photovoltaic absorber underneath is highly demanded to simplify the fabrication process of PV devices.

In this work, we present a universal highly-conductive ETL for *c*-Si and OPV devices. Titanium oxynitride (TiO$_x$N$_y$) deposited by ALD, featuring suitable electronic properties is demonstrated to be an efficient ETL for the different PV devices. By the implementation of electron-selective TiO$_x$N$_y$ contact, a best PCE of 22.3% and 17.02% is achieved on *c*-Si and OPV devices, respectively, with a simplified fabrication processing without thermal annealing.

TiO$_x$N$_y$ films were deposited by remote-plasma ALD, which offers atomic control over its thickness with low plasma damage. Figure 1a displays the high-resolution X-ray photoelectron spectroscopy (XPS) core-level spectrum of Ti 2p in the film, consisting of TiO$_2$, TiN and TiON peaks. The elemental concentration in as-deposited film was calculated to be 38% titanium (Ti), 43% oxygen (O), and 19% nitrogen (N). Here we define as-deposited film with a non-stoichiometric chemical formula, TiO$_x$N$_y$, following the previous reports on the ALD deposition of TiO$_x$N$_y$ films.[26,27] The optical band gap of TiO$_x$N$_y$ was determined to be ~ 3.4 eV, which was extracted via ultraviolet-visible (UV-vis) spectroscopy using T_{auc} plots (see Supplementary Figure S1). From the onset of the ultraviolet photoelectron spectroscopy (UPS) spectrum at the high binding energy after surface etching, as shown in **Figure 1b**, the work function of TiO$_x$N$_y$ is determined to be ~ 4.3 eV. The E$_f$ - E$_v$ value (~ 3.3 eV) is obtained from the cutoff in UPS spectrum. The sub-bandgap defect band observed between the valence band and Fermi energy might be attributed to the surface-etching damage, because no sub-band-gap defect band is observed before surface etching. Hall effect measurement reveals that the TiO$_x$N$_y$ film behaves as an *n*-type semiconductor, featuring a low resistivity of ~ 1.5 × 10^{-2} Ω.cm and a high electron density of 4.3 × 10^{22} cm^{-3}. Both the conductivity and electron density of TiO$_x$N$_y$ are much higher than those of

TiO_2,[28,29] which can be attributed to the presence of a quasi-metallic TiN phase, featuring a high conductivity and high electron density.[30] The high electron concentration of TiO_xN_y is essential to yield better electron selectivity on device level, which will be discussed later.
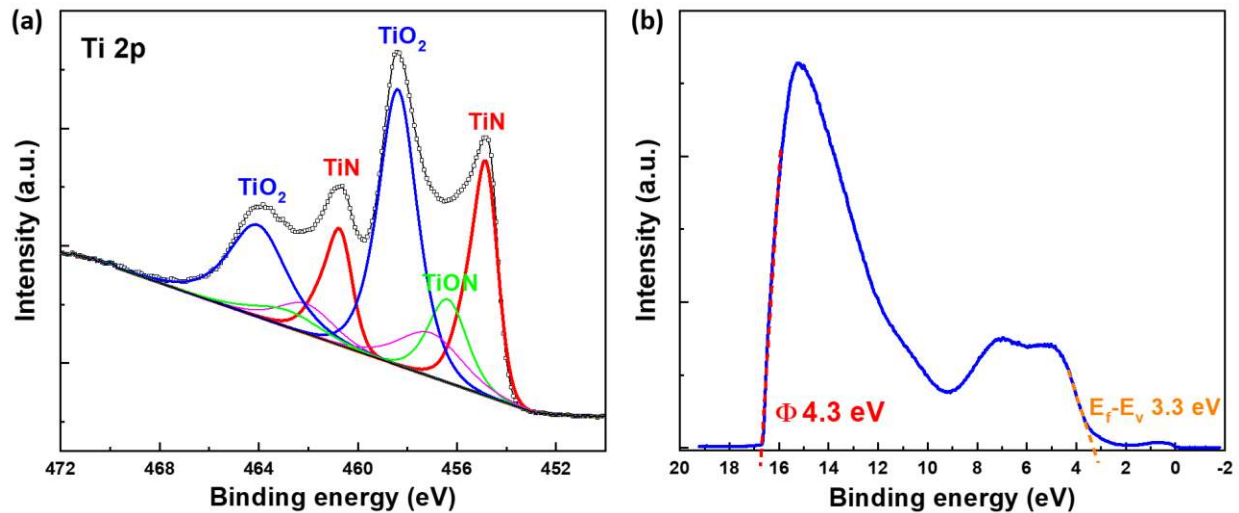

Figure 1. (a) XPS core-level spectra of Ti 2p for TiO_xN_y deposited by ALD; (b) The UPS spectrum of TiO_xN_y using He-I excitation.

Figure 2a sketches a *c*-Si solar cell featuring a full-area, electron-selective TiO_xN_y rear contact. Such devices (2×2 cm^2), were prepared on high-quality *n*-type float zone (FZ) silicon substrates, featuring a random-pyramid textured front surface. The front boron-diffused p^+ emitter was passivated by ALD Al_2O_3, and then capped with a double-layer antireflection stack of SiN_x/MgF_2. A full-area TiO_xN_y (~ 3.8 nm) and *a*-Si:H/TiO_xN_y (~ 4.0/2.5 nm) contacts were implemented at the rear for electron collection (see cross-sectional TEM images in Fig. 2b and 2c), enabling a low process complexity without diffusion and contact patterning steps. Thin, intrinsic amorphous silicon films (*a*-Si:H) are well-known for achieving excellent passivation on *c*-Si surface. A reference cell with Al rear contact was fabricated for comparison.
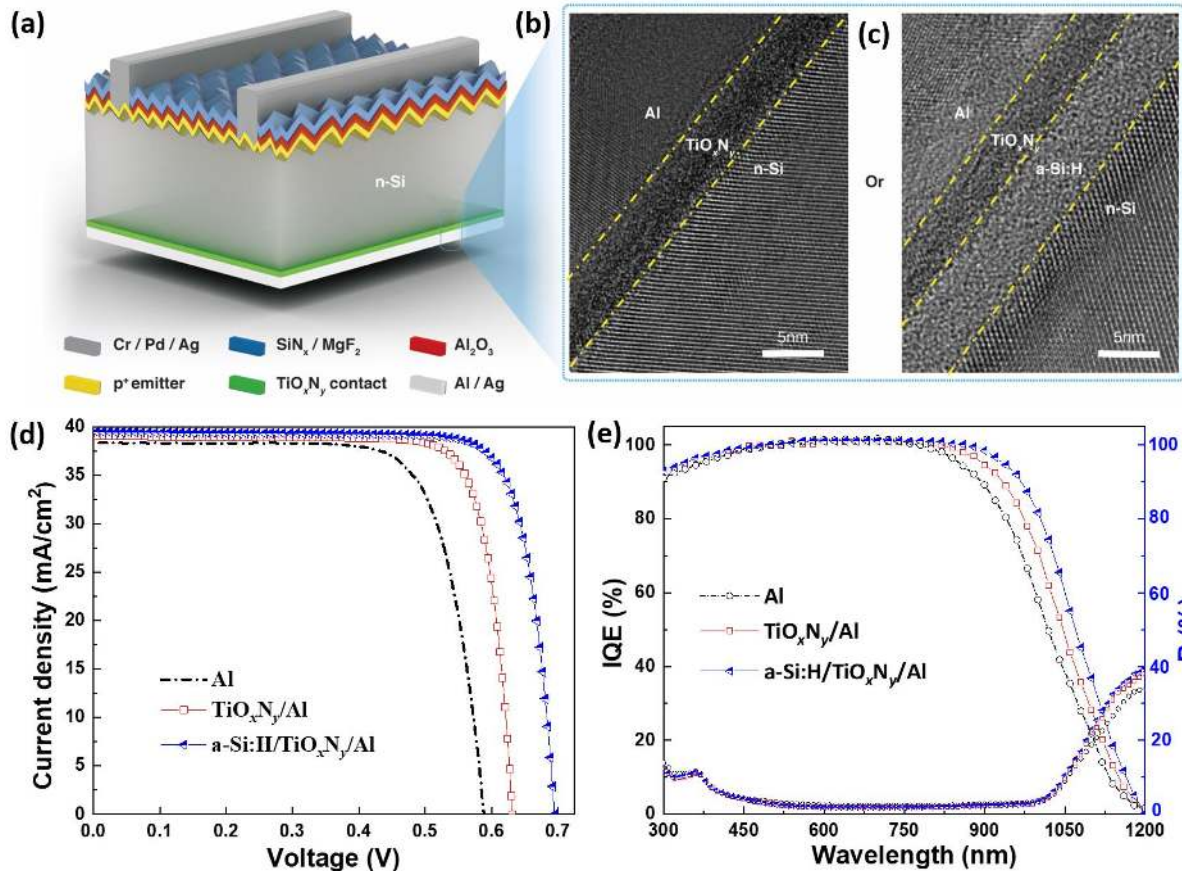
Figure 2. (a) The sketch of *n*-Si solar cell featuring a full-area TiO_xN_y and *a*-Si:H/TiO_xN_y rear contacts; Cross-sectional TEM images of (b) TiO_xN_y and (c) *a*-Si:H/TiO_xN_y contact; (d) Light *J-V* curves under AM 1.5G and (e) corresponding IQE and reflectance of *n*-Si solar cells with a full-area Al, TiO_xN_y, *a*-Si:H/TiO_xN_y rear contacts.

The illuminated current-density/voltage (*J-V*) curves of *c*-Si solar cells with different rear contacts under the standard one-sun illumination are shown in Figure 2d, and the photovoltaic parameters, pseudo *FF* (*pFF*) and series resistance (*R_s*) of the best devices are listed in Table 1. The reference cell with a simple Al rear contact shows a poor PCE of 16.8%, featuring a low V_{oc} of 589 mV and FF of 74.6%, which can be attributed to the lack of surface passivation and the presence of a large Schottky barrier height (> 0.7 eV) at the rear *n*-Si/Al interface,[31] resulting in a high carrier recombination velocity and a non-ohmic contact, respectively. When a thin TiO_xN_y

interlayer is inserted between n-Si and Al interface, all the photovoltaic parameters, especially the FF and V_{oc}, are significantly enhanced, resulting in an improved PCE close to 20%. This indicates that simultaneously a reduction of ρ_c and carrier recombination velocity occurs due to the presence of TiO_xN_y interlayer. The result is consistent with the internal quantum efficiency (IQE) measurement (Figure 2e), which indicates that the quantum efficiency is significantly improved in the near-infrared range (800-1200 nm) for the device with TiO_xN_y contact, compared to that of Al contact. By further introducing an a-Si:H passivation interlayer between n-Si and TiO_xN_y interface, the device PCE is dramatically boosted to 22.3%, featuring in a V_{oc} of 698 mV, a FF of 80.8% and a J_{sc} of 39.5 mA/cm^2. The IQE results indicate that the quantum efficiency in the near-infrared range is further improved, which reflects that carrier recombination velocity is significantly reduced at the rear side. By implementation of a-Si:H/TiO_xN_y stack at the rear side, an absolute V_{oc}, FF and J_{sc} gain of 109 mV, 6.2% and 1.3 mA/cm^2 is achieved, respectively, resulting in an absolute PCE gain of 5.5%. By collecting the photovoltaic parameters from eight devices, an average PCE of 22.0% is obtained on the n-Si solar cells with a-Si:H/TiO_xN_y contact, which demonstrates the high reproducibility and reliability of a-Si:H/TiO_xN_y contact (see Supplementary Figure S2). After exposure to ambient air for 3 months, the champion device exhibits almost no PCE degradation (see Supplementary Table S1), which further demonstrates the high stability of n-Si solar cells with a-Si:H/TiO_xN_y contact.

Table 1. Photovoltaic parameters of the best n-Si solar cells with Al, TiO_xN_y and a-Si:H/TiO_xN_y contacts.

Rear contact type	V_{oc} (mV)	J_{sc} (mA/cm^2)	FF (%)	η (%)	pFF (%)	R_s ($\Omega.cm^2$)
Al	589	38.2	74.6	16.8	80.6	1.15
TiO_xN_y	629	38.8	81.7	19.9	83.4	0.38
a-Si: H/TiO_xN_y	698	39.5	80.8	22.3	82.6	0.45

A significant PCE enhancement in c-Si solar cells has been proven by the implementation of a full-area TiO_xN_y and a-Si:H/TiO_xN_y contacts. The improvement on PCE is mainly attributed to the significant V_{oc} and FF enhancement, which indicates that TiO_xN_y contacts simultaneously reduce the carrier recombination velocity and ρ_c at the rear side. Figure 3a shows the dependence of ρ_c on the TiO_xN_y thickness for the n-Si/TiO_xN_y/Al and n-Si/a-Si:H/TiO_xN_y/Al heterocontacts, which were extracted by the Cox and Strack method.[32] With an ultrathin TiO_xN_y interlayer (2.5 nm), the n-Si/TiO_xN_y/Al heterocontact exhibits a very low ρ_c of ~ 12 mΩ.cm^2, which is much lower than that of n-Si/Al contact (> 500 mΩ.cm^2).[9] With a thicker TiO_xN_y of 3.8 and 5.0 nm, the ρ_c increases to ~ 17 and ~ 29 mΩ.cm^2, respectively, demonstrating a weak thickness dependence, compared to that of TiO_2 and TaN_x contacts with a high bulk resistance.[10,15] After inserting an a-Si: H passivation interlayer, ρ_c of all the n-Si/a-Si:H/TiO_xN_y/Al heterocontacts under different TiO_xN_y thickness increase dramatically, which might be attributed to the presence of a tunnel resistance through the intrinsic a-Si:H passivation layer. Nevertheless, with an ultrathin TiO_xN_y capping layer (~ 2.5 nm) over a-Si:H, the ρ_c of n-Si/a-Si:H/TiO_xN_y/Al heterocontact is ~ 78 mΩ.cm^2, which is higher than the best reported ρ_c of conventional SHJ electron contact measured by transfer length method (~ 30 mΩ.cm^2).[33,34] Note, however, that the ρ_c extracted by the Cox and Strack method can be considered as the upper limit value for the a-Si:H/TiO_xN_y/Al heterocontact, because it comprises the resistance of the front a-Si:H/TiO_xN_y/Al and rear n-Si/Al interfaces as well as the a-Si:H and TiO_xN_y bulk resistivity. Thanks to the reduced ρ_c at the n-Si/TiO_xN_y/Al and n-Si/a-Si:H/TiO_xN_y/Al heterocontacts, which are the well below the ρ_c threshold (≤ 100 mΩ.cm^2) of a full-area contact for high efficiency c-Si solar cells,[15,35] R_s and FFs of the corresponding devices are significantly improved, as shown in Table 1.
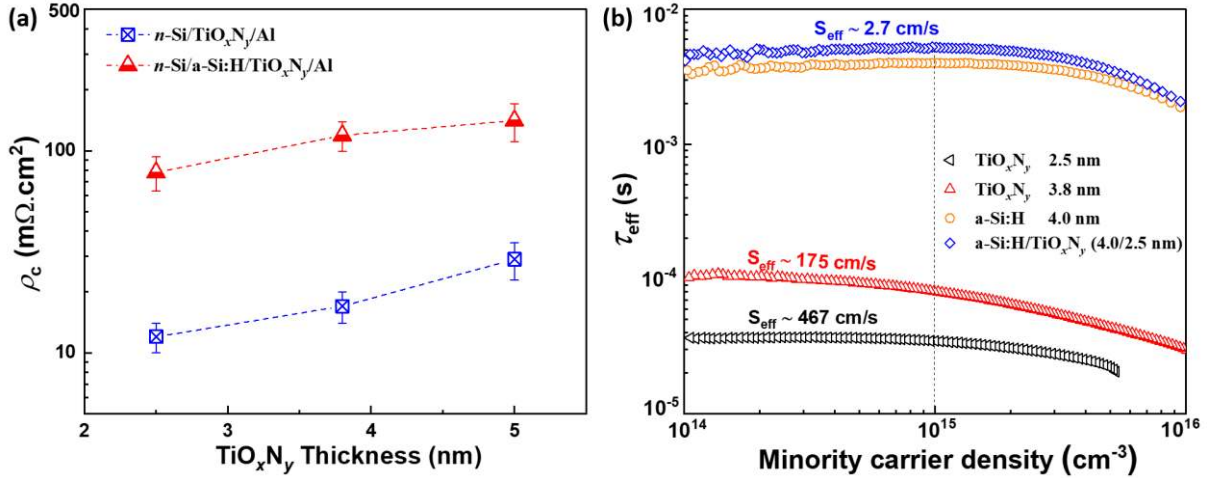
Figure 3. (a) Dependence of ρ_c on the TiO$_x$N$_y$ thickness for the *n*-Si/TiO$_x$N$_y$/Al and n-Si/a-Si:H/TiO$_x$N$_y$/Al heterocontacts; (b) Injection-level-dependent effective lifetimes of *n*-Si (1.0 Ω cm) passivated by TiO$_x$N$_y$, a-Si:H and a-Si:H/TiO$_x$N$_y$ stack.

Figure 3b shows the carrier-injection dependent effective carrier lifetimes (τ_{eff}) of *n*-Si (1.0 Ω cm) respectively passivated by TiO$_x$N$_y$, a-Si:H and the a-Si:H/TiO$_x$N$_y$ stack. Thin TiO$_x$N$_y$ films (2.5 and 3.8 nm) result in relatively poor surface passivation, exhibiting a low τ_{eff} of 30 and 80 μs at the minority carrier density of 1×10^{15} cm^{-3}, respectively. The corresponding effective surface recombination velocities (S_{eff}) are calculated to be 467 and 175 cm/s, which are nevertheless much lower than that of *n*-Si/Al direct contact (10^6-10^7 cm/s, without any back surface field).[10] Therefore, with the 3.8 nm TiO$_x$N$_y$ interlayer, which simultaneously reduces the S$_{eff}$ and ρ_c at the rear side, the V_{oc}, J_{sc} and *FF* of the device are significantly improved. However, the surface passivation quality of thin TiO$_x$N$_y$ layers is too poor to achieve a high PCE. Thin intrinsic a-Si:H films, as commonly employed for SHJ solar cell fabrication, acts as a very efficient passivation interlayer (τ_{eff} ~ 4000 μs, open circle in Figure 3b). As a consequence, we can achieve excellent surface passivation with a-Si:H/TiO$_x$N$_y$ (4.0/2.5 nm) stack, achieving an τ_{eff} and S$_{eff}$ of 5200 μs and 2.7 cm/s, respectively. Meanwhile, the ρ_c of the *n*-Si/a-Si:H/TiO$_x$N$_y$/Al heterocontact is

maintained at an acceptable value for a full-area contact, as shown in Figure 3a. With the optimal a-Si:H/TiO$_x$N$_y$ stack, simultaneously offering excellent surface passivation and a moderate ρ_c, the V_{oc} and J_{sc} are dramatically improved to 698 mV and 39.5 mA/cm^2, respectively, while the *FF* drops slightly to 80.8%, resulting in a significantly PCE enhancement to 22.3%. Although the 22.3% efficient sets a new benchmark for *c*-Si solar cells featuring a full-area dopant-free electron-selective contact, it is still far below the champion devices of PERC (24.7%), SHJ (25.1%) and TOPCon (25.8%),[36] as listed in Supplementary Table S2. Further improvements can be achieved by implementing a selective emitter at the front side, which will reduce the front carrier recombination loss significantly.

Previously, it was found that ALD-deposited TiO$_2$ combined with a-Si:H passivation interlayer leads to an s-shape *J-V* curve of *c*-Si device,[37] indicating a poor electron selectivity of the a-Si:H/TiO$_2$ stack. Contrastingly, the SiO$_2$/TiO$_2$ stack was proven to be an excellent electron-selective contact for *c*-Si solar cells, provided that thermal annealing at ~350°C was applied.[8,10] It is interesting that a-Si:H/TiO$_x$N$_y$ stack exhibits excellent electron selectivity without thermal annealing. Here we investigate the underlying mechanism by calculating the band alignment at the *n*-Si/a-Si:H/TiO$_x$N$_y$ interface as a function of the electron density of TiO$_x$N$_y$, using the free numerical simulation tool AFORS-HET.[38] Key parameters of *n*-Si, a-Si:H and TiO$_x$N$_y$ for the simulation are summarized in Table S3. The results demonstrate that the barrier width and height at the a-Si:H/*n*-Si interface significantly rely on the electron density of the capping TiO$_x$N$_y$ (see Supplementary Figure S3a). A high electron density can reduce the Schottky barrier width and height effectively, which benefits the electron transport at the *n*-Si/a-Si:H/TiO$_x$N$_y$ heterocontact. Under a low electron density (e.g. < 2×10^{22} cm^{-3}), the simulated *J-V* curves exhibit an S-shape (see Supplementary Figure S3b), which is quite similar to that of devices with an a-Si:H/TiO$_2$

contact.[37] So the poor electron selectivity of a-Si:H/TiO$_2$ contact can be attributed to the low electron density of TiO$_2$ (typically in the range of 10^{16}-10^{17} cm^{-3}).[28] This finding provides valuable insight in the development of new effective carrier selective contacts that are compatible with a-Si:H passivation interlayers.

ZnO is widely used as an ETL for OPV devices with inverted architectures.[39,40] Deposition of the compact ZnO film is often conducted by spin coating the precursor formulation at room temperature followed by a relatively high temperature thermal annealing step at > 200 °C for a prolonged period of time.[41-44] Unfortunately, the resulting ZnO ETL suffers from poor photo-stability due to its intrinsic ultraviolet (UV) absorption characteristics, which results in oxygen desorption and increased shunts.[45,46] For these reasons recent efforts have been increasingly focused on developing alternative ETLs with suitable electronic properties and simple and scalable processing (*e.g.*, without high-temperature thermal annealing).

Inspired by the promising electronic properties of TiO$_x$N$_y$ and the positive impact on the operating characteristics of Si PV cells discussed previously, we investigate its potential as ETL in inverted OPVs cells (Figure 4a). Firstly, we optimize the thickness of TiO$_x$N$_y$ ETL in OPVs featuring a bulk-heterojunction (BHJ) consisting of the ternary system PM6:Y6:PC$_{71}$BM (Figure 4b). Control devices with solution-processed ZnO ETL were prepared in parallel for comparison. We note that the TiO$_x$N$_y$ ETL was used without thermal annealing, whereas ZnO was annealed at 200°C for 30 min in air. Figure 4c shows the *J–V* curves of the best performing OPV cells with TiO$_x$N$_y$ and ZnO ETLs, and the photovoltaic parameters (best and average) are listed in Table 2. The control device featuring the ZnO ETL exhibits a maximum PCE of 16.10%, with a V_{oc} of 0.84 V, a J_{sc} of 25.70 mA/cm^2, a FF of 74.49%. In contrast, the PCE for the TiO$_x$N$_y$-based cell is boosted to 17.02%, a result attributed to higher FF and J_{sc} of 76.41 and 26.18 mA/cm^2, respectively. The

higher FF is attributed to the reduced R_s from 2.91 to 2.26 $\Omega.cm^2$. The electrochemical impedance spectroscopy (EIS) was performed on the devices in the dark (with a bias voltage equal to V_{oc}) to investigate the interface resistance of the devices. Nyquist plots were fitted using the equivalent circuit model (Figure S4), and the obtained parameters are shown in Table S4. We find that the interface resistances (R_2) of the devices with TiO_xN_y (22.5 Ω) is much lower than that of device with ZnO ETLs (30.8 Ω). Therefore, the reduced R_s can be attributed to a higher bulk conductivity of TiO_xN_y and a lower interface resistance. Figure 4d displays the external quantum efficiency (EQE) spectra and reflectance of the PM6:Y6:PC_{71}BM cells incorporating TiO_xN_y and ZnO ETLs. The integral current density values deduced from the EQE spectra are well matched with the values obtained from the $J–V$ measurements within ±3%. The device with TiO_xN_y ETL exhibit higher photo-responses from 522 to 638 nm, and 670 to 811 nm, compared to that of device with ZnO ETL, which might be attributed to a lower reflectance (dash line in Figure 4d) and a smaller bimolecular recombination in TiO_xN_y based device (discussed later). These enhanced EQE features contribute to calculated current density (J_{cal}) increase from 25.17 mA/cm^2 (ZnO) to 25.58 mA/cm^2 (TiO_xN_y), which is in good agreement with the measured J_{sc} values.

Table 2. The best and average (calculated from 15 devices) photovoltaic parameters of the OPV devices featuring a conductive TiO_xN_y or solution-processed ZnO ETL.

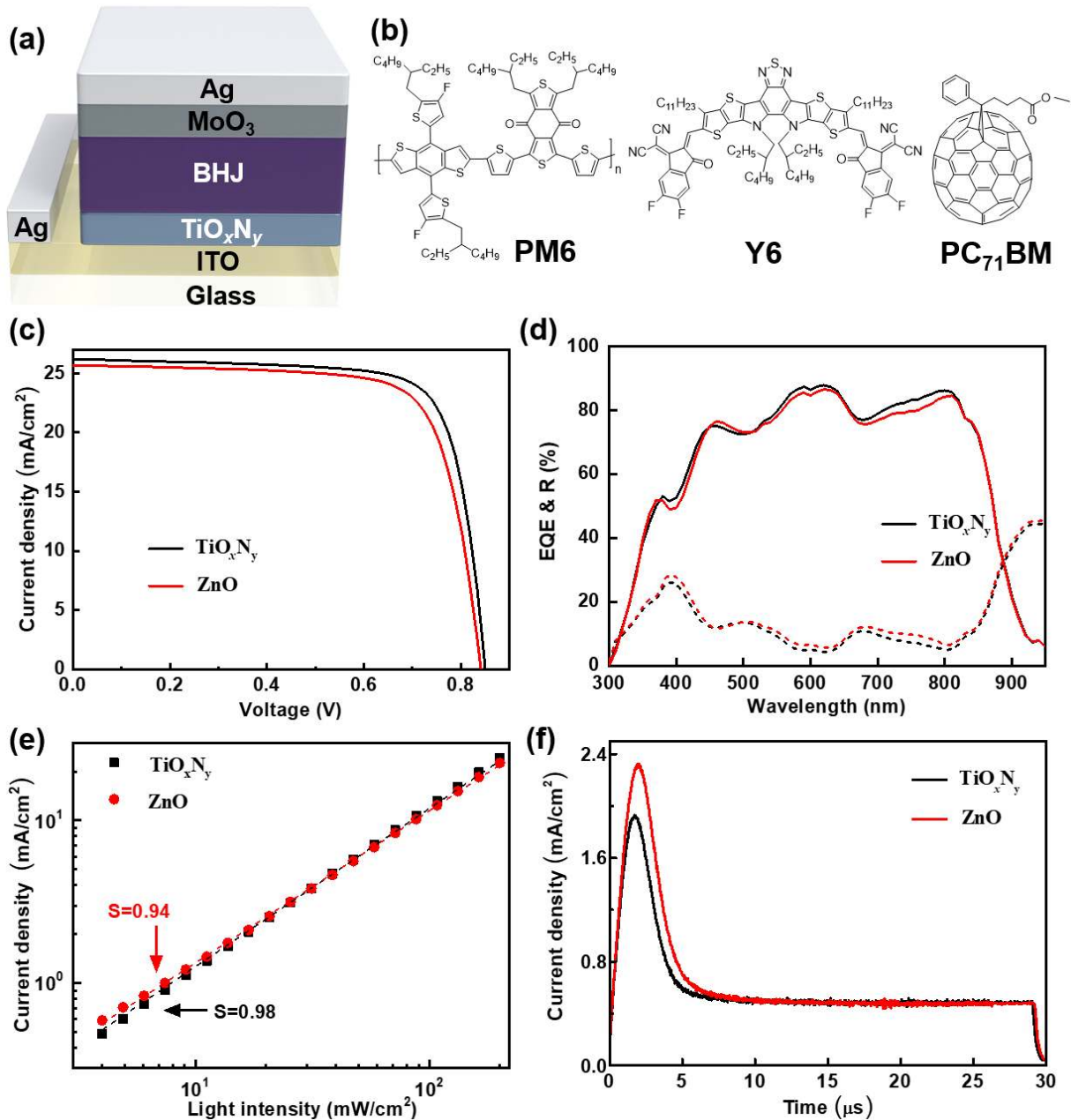| ETL	V_{oc} (V)	J_{sc} (mA/cm^2)	J_{cal} (mA/cm^2)	FF (%)	PCE (%)	R_s ($\Omega.cm^2$)
TiO_xN_y (15 nm)	0.85 (0.84±0.01)	26.18 (25.91±0.20)	25.58	76.41 (75.74±0.4)	17.02 (16.61±0.31)	2.26
ZnO (30 nm)	0.84 (0.83±0.01)	25.70 (25.38±0.27)	25.17	74.49 (73.92±0.41)	16.10 (15.81±0.33)	2.91

Fig. 4. (a) The structure of OPV device featuring a TiO$_x$N$_y$ ETL (15 nm); (b) chemical structures of PM6, Y6, and PC$_{71}$BM; (c) Light *J-V* curves under AM 1.5G and (d) corresponding EQE (solid lines) and reflectance (dash lines) of OPV devices with TiO$_x$N$_y$ and ZnO ETLs; (e) Light intensity dependence of *J*$_{sc}$ and (f) photo-CELIV curves measured for the same cells.

We also examined the light-intensity dependence of J_{sc} to estimate the bimolecular recombination losses in the devices with different ETLs (Figure 4e). The relationship between J_{sc} and incident light intensity (P_{light}) can be described as $J_{sc} \propto (P_{light})$.[47] Here, S is equal to 1 if all free carriers are collected at the corresponding electrodes without any recombination, while a value of S < 1 indicates the presence of bimolecular recombination. For TiO_xN_y ETL-based cells a S = 0.98 is extracted, compared to 0.94 for the devices with ZnO. This negligible bimolecular recombination demonstrates the superiority of the highly-conductive TiO_xN_y ETL in facilitating extraction of photo-generated charge carriers more efficiently, compared to ZnO ETL. The carrier mobility in OPVs featuring TiO_xN_y and ZnO ETLs were also investigated using the photo-induced charge-carrier extraction with linearly increasing voltage (Photo-CELIV) (Figure 4f). Evidently, different transient currents and characteristic features are recorded. The corresponding mobility was calculated using:[48]

$$\mu=2d^2/(3At^2_{max}(1+0.36\Delta j/j_0)) \tag{1}$$

where d is BHJ layer thickness, A is the voltage rise speed of the applied voltage pulse, t_{max} is the time to reach the extraction current maximum, and Δj and j_0 are the shifting and initial current step, respectively. Evidently, the device with TiO_xN_y exhibits a carrier mobility of 4.52×10^{-4} cm^2 V^{-1} s^{-1}, which is 1.6 times higher than that of ZnO-based device (2.88×10^{-4} cm^2 V^{-1} s^{-1}). These results suggest that the utilization of TiO_xN_y ETL facilitates a better electron transport/extraction from within the BHJ than the conventional ZnO ETL.

In summary, conductive TiO_xN_y films deposited by ALD have successfully developed as an efficient ETL for c-Si and organic photovoltaic devices. By the implementation of the optimal TiO_xN_y ETL, a high PCE of 22.3% and 17.02% has been achieved on *c*-Si and OPV devices, respectively. Compared to the commonly used ETLs made of transition metal oxides, the process

complexity of photovoltaic devices with TiO_xN_y ETL is simplified by eliminating thermal annealing step. Furthermore, TiO_xN_y deposited by ALD exhibits the merit of high uniformity on a large area, compared to that of solution-processed ETLs, which is very attractive for large-size OPV devices fabrication. The entire body of results presented and analyzed highlight the tremendous potential of TiO_xN_y ETL for photovoltaic devices.

Experimental Section

TiO$_x$N$_y$ films deposition and characterization. TiO$_x$N$_y$ films were deposited at 250°C by remote-plasma ALD (Oxford Instrument) using the oxygen-free tetrakis(dimethylamino)titanium (TDMAT) as the titanium precursor and NH$_3$/H$_2$ mixture as the reactant gas. The TDMAT precursor bottle is kept at 50 °C by a temperature controller, and the tube from the precursor bottle to the chamber is heated to 60 °C to prevent condensation of the precursor gas. One cycle ALD deposition consists of a TDMAT precursor exposure for 1 s, an argon purge for 5 s, a NH$_3$/H$_2$ plasma for 10 s and an argon purge for 5 s, resulting in a growth rate of ~ 0.1 nm/cycle. The oxygen source can be ascribed to the oxygen residuals in the reactor as well as the oxygen impurity in the reactive and purge gases.

The chemical bonding states of TiO$_x$N$_y$ films were characterized by high-resolution XPS (Kratos Axis, Kratos Analytical Ltd.) integrated with a monochromatic Al Kα X-ray source (1486.6 eV). High-resolution XPS spectra were acquired at fixed analyzer pass energies of 20 and 160 eV, and quantified using empirically derived relative sensitivity factors provided by the manufacturer. C 1s peak at 285.0 eV was used to calibrate the binding energies. XPS spectra were analyzed using CasaXPS, a commercially available software. The work function of the TiO$_x$N$_y$ film was determined by UPS (Kratos Axis Ultra) using a He-I excitation (21.22 eV) after surface etching with Ar$^+$ ions. The optical bandgap of the TiO$_x$N$_y$ film was determined using a UV-vis spectrometer (Carry 7000, Agilent). Hall-effect measurement was performed on a Lake Shore analyzer at room temperature in the dark under a 10 kG magnetic field. The sample (10 × 10 mm^2) was prepared in the Van der Pauw geometry, and conductive silver paste was used for preparing the contacts. Ohmic behavior of the silver contacts was confirmed by checking the linear variation in the *J-V* characteristics.

Contact resistivity and surface passivation of TiO$_x$N$_y$ on c-Si. The ρ_c of *n*-Si/TiO$_x$N$_y$ and *n*-Si/a-Si:H/TiO$_x$N$_y$ heterocontacts were measured using the Cox and Strack method.[32] Test structures were prepared by depositing different thickness of TiO$_x$N$_y$ or a-Si:H/TiO$_x$N$_y$ stack on the front side of *n*-type *c*-Si substrate (0.3 Ω·cm), following by evaporating Al circular contacts (300 nm) with different diameters through a shadow mask. The rear side was metallized by a full-area thermally evaporated Al (500 nm). The a-Si: H passivation interlayer with a fixed thickness of 4.0 nm was deposited in a multi-chamber PECVD system at 200°C. ρ_c were extracted by fitting the trend of resistance versus diameter of the front contacts, as detailed in the previous reports.[8,15,16]

The surface passivation of TiO$_x$N$_y$ films on *c*-Si was evaluated using the quasi-steady-state photoconductance (QSSPC) technique. A symmetrical structure was prepared by depositing TiO$_x$N$_y$ or a-Si:H/TiO$_x$N$_y$ stack on both sides of cleaned *n*-type *c*-Si (2.5 Ω·cm, 250 µm) wafers, allowing the τ_{eff} measurement with a lifetime tester (WCT-120, Sinton Instruments). S$_{eff}$ was calculated using the obtained τ_{eff} value by:

$$\frac{1}{\tau_{eff}} = \frac{1}{\tau_{bulk}} + \frac{2S_{eff}}{W}$$

where τ$_{bulk}$ is the bulk lifetime of the *n*-type *c*-Si wafer, and *W* the wafer thickness. Since high quality float-zone wafers were used, the τ$_{bulk}$ was set to infinite. Therefore, the obtained *S*$_{eff}$ represents an upper limit value.

Silicon solar cells fabrication. c-Si solar cells with electron-selective TiO$_x$N$_y$ or a-Si:H/TiO$_x$N$_y$ heterocontacts were fabricated on *n*-type *c*-Si wafers (1.0 Ω·cm, ~ 175 µm). After surface damage etching in an alkaline solution and RCA cleaning, SiN$_x$ mask layer (~ 120 nm) was deposited on both sides by low-pressure chemical vapour deposition (LPCVD). The active cell area (2 × 2 cm^2) was then defined using photolithography, and followed by RIE etching. After texturing with

random pyramids and RCA cleaning, the front p^+ emitter (~ 120 Ω/sq) was prepared by boron diffusion in a tube furnace. ALD Al_2O_3 passivation layer (20 nm) and PECVD SiN_x (55 nm) antireflection layer were deposited continuously on the top of p^+ emitter, followed by a forming gas annealing at 400°C for 30 mins. After etching the rear SiN_x by HF fuming, TiO_xN_y film (3.8 nm) or a-Si:H/TiO_xN_y (4/2.5 nm) stack was deposited immediately, and then metallized by a thermally evaporated Al/Ag (20/1000 nm). The front contact areas were opened photolithographically using a buffered HF solution to remove the Al_2O_3/SiN_x stack. The front fingers were formed by lift-off after thermally evaporation of Cr/Pd/Ag (30/30/30 nm) stack, subsequently thickened using silver electroplating. Finally, a double-reflection layer MgF_2 (100 nm) was thermally evaporated on the front side.

Organic solar cells fabrication. PM6 and Y6 blend materials were purchased from Solarmer Inc., and $PC_{71}BM$ acceptor were purchased from SolenneBV Inc. Chloroform (CF) and 1-chloronaphthalene (CN) were obtained from Sigma-Aldrich. PM6: Y6: $PC_{71}BM$ were dissolved in CF: CN (99.5:0.5, volume ratio) solution with a PM6 donor concentration of 7 mg/ml. The ZnO precursor solution was prepared by dissolving 200 mg of zinc acetate dihydrate in 2 mL of 2-Methoxyethanol and 60 ul of 2-Aminoethanol. The inverted OPV device structure is ITO/ETL/Active Layers/MoO_x/Ag. ITO substrates were cleaned with detergent water, deionized water, acetone and isopropyl alcohol in an ultrasonic bath sequentially for 20 min. TiO_xN_y ETL (15 nm) was then deposited on top of ITO substrates by ALD, followed by a UV-O_3 treatment step for 10 min. For comparison, ZnO precursor solution was spin-coated onto the same substrates and then dried on a hot plate at 200 °C for 30 minutes. After transferring into nitrogen-filled glove box, the PM6: Y6: $PC_{71}BM$ blend solutions were spin coated at 3000 rpm to obtain an optimal thickness of ~110 nm. The device fabrication was completed by thermal evaporation of

MoO$_x$ hole-transport layer (7 nm) and Ag electrode (100 nm) continuously at a pressure of less than 2×10^{-6} Pa. The active area of the devices was defined to be 0.1 cm^2 through a shadow mask.

Photovoltaic devices characterization. The light *J-V* characteristics of the *c*-Si solar cells were measured using a LED-based solar simulator (SINUS-220, WaveLabs GmbH) under standard one-sun conditions (25°C, 1000 W/m^2). The light intensity was calibrated using a reference cell obtained from Fraunhofer ISE CalLab. The EQE and reflection of *c*-Si solar cells were characterized by the LOANA system (pv-tools, GmbH), which include an EQE measurement setup that provides monochromatic light between 280-1600 nm. The cross sections of the *n*-Si/TiO$_x$N$_y$/Al and *n*-Si/a-Si:H/TiO$_x$N$_y$/Al heterocontacts were observed by high-resolution TEM (HRTEM, FEI Titan 80-300ST). *J–V* measurements of OPV devices were performed in a N$_2$ filled glove box using a Keithley 2400 source meter and an Oriel Sol3A Class AAA solar simulator calibrated to 1 sun, AM1.5G, with a KG-5 silicon reference cell certified by Newport. EQE was characterized using an EQE system (PV measurement Inc.). Measurements were performed at zero bias by illuminating the device with monochromatic light supplied from a Xenon arc lamp in combination with a dual-grating monochromator. The number of photons incident on the sample was calculated for each wavelength by using a silicon photodiode calibrated by The National Institute of Standards and Technology (NIST). Light-intensity dependence measurements were performed with PAIOS instrumentation (Fluxim) (steady-state and transient modes). Photo-CELIV measurements (ramp rate 200 V ms-1, delay time: 50 μs, offset voltage: 0 V, light-pulse length: 100 μs) were also performed using PAIOS with the maximum power (200 mW cm^{-2}) of the LED source.

Supporting Information
Supporting Information is available from the Wiley Online Library or from the author.

Acknowledgements

References

[1] Photovoltaics Report, Fraunhofer Institute for Solar Energy Systems, November **2019**.

[2] J. Benick, B. Hoex, M. Sanden, W. Kessels, O. Schultz, S. Glunz, *Appl. Phys. Lett.* **2008**, 92, 253504.

[3] T. Allen, J. Bullock, X. Yang, A. Javey, and S. De Wolf, *Nat. Energy* **2019**, 4, 914-928.

[4] J. Melskens, B. H. Loo, B. Macco, L. E. Black, S. Smit, W. M. M. Kessels, *IEEE J. Photovolt.* **2018**, 8, 373-388.

[5] J. Schmidt, R. Peibst, R. Brendel, *Sol. Energy Mater. Sol. Cells* 2018, **187**, 39-54.

[6] K. Yoshikawa, W. Yoshida, T. Irie, H. Kawasaki, K. Konishi, H. Ishibashi, T. Asatani, D. Adachi, M. Kanematsu, H. Uzu, K. Yamamoto, *Sol. Energy Mater. Sol. Cells* **2017**, 173, 37-42.

[7] F. Haase, C. Hollemann, S. Schäfer, A. Merkle, M. Rienäcker, J. Krügener, R. Brendel, R. Peibst, *Sol. Energy Mater. Sol. Cells* **2018**, 186, 184-193.

[8] X. Yang, K. Weber, Z. Hameiri, S. De Wolf, *Prog. Photovolt.: Res. Appl.* **2017**, 25, 896-904 (2017).

[9] Y. Wan, C. Samundsett, J. Bullock, M. Hettick, T. Allen, D. Yan, J. Peng, Y. Wu, A. Javey, A. Cuevas, *Adv. Energy Mater.* **2017**, 7, 1601863.

[10] X. Yang, Q. Bi, H. Ali, K. Davis, W. V. Schoenfeld, K. Weber, *Adv. Mater.* **2016**, 28, 5891-5897.

[11] C. Battaglia, X. Yin, M. Zheng, I. D. Sharp, T. Chen, S. McDonnell, A. Azcatl, C. Carraro, B. Ma, R. Maboudian, R. M. Wallace, A. Javey, *Nano Lett.* **2014**, 14, 967-971.

[12] J. Dreon, Q. Jeangros, J. Cattin, J. Haschke, L. Antognini, C. Ballif, M. Boccard, *Nano Energy* **2020**, 70, 104495.

[13] M. Bivour, J. Temmler, H. Steinkemper, M. Hermle, *Sol. Energy Mater. Sol. Cells* **2015**, 142, 34-41.

[14] L. G. Gerling, S. Mahato, A. Morales-Vilches, G. Masmitja,P. Ortega, C. Voz, R. Alcubilla, J. Puigdollers, *Sol. Energy Mater. Sol. Cells* **2016**, 145, 109-115.

[15] X. Yang, E. Aydin, H. Xu, J. Kang, M. Hedhili, W. Liu, Y. Wan, J. Peng, C. Samundsett, A. Cuevas, A., S. de Wolf, *Adv. Energy Mater.* **2018**, 8, 1800608.

[16] J. Bullock, Y. Wan, Z. Xu, S. Essig, M. Hettick, H. Wang, W. Ji, M. Boccard, A. Cuevas, C. Ballif, A. Javey, *ACS Energy Lett.* **2018**, 3, 508-513.

[17] P. K. Nayak, S. Mahesh, H. J. Snaith, D. Cahen, *Nature Rev. Mater.* **2019**, 4, 269-285.

[18] N. Gasparini, A. Salleo, I. McCulloch, D. Baran, *Nature Rev. Mater.,* **2019**, 4, 229-242.

[19] Q. Liu, Y. Jiang, K. Jin, J. Qin, J. Xu, W. Li, J Xiong, J. Liu, Z. Xiao, K. Sun, S. Yang, X. Zhang, L. Ding, *Sci. Bulletin* **2020**, 65, 272-275.

[20] Y. Lin, Y. Firdaus, M. Nugraha, F. Liu, S. Karuthedath, A. Emwas, W. Zhang, A. Seitkhan, M. Neophytou, H. Faber, E. Yengel, I. McCulloch, L. Tsetseris, F. Laquai, T. D. Anthopoulos. *Adv. Sci.* **2020**, 1903419.

[21] L. Meng, Y. Zhang, X. Wan, C. Li, X. Zhang, Y. Wang, X. Ke, Z. Xiao, L. Ding, R. Xia, H. Yip, Y. Cao, Y. Chen, *Science* **2018**, 361, 1094-1098.

[22] C. E. Small, S. Chen, J. Subbiah, C. M. Amb, S.-W. Tsang, T.-H. Lai, J. R. Reynolds and F. So, *Nat. Photonics* **2011**, 6, 115-120.

[23] X. Bao, L. Sun, W. Shen, C. Yang, W. Chen and R. Yang, *J. Mater. Chem. A* **2014**, 2, 1732-1737.

[24] F. Huang, H. B. Wu, D. Wang, W. Yang and Y. Cao, *Chem. Mater.* **2004**, 16, 708-716.

[25] Z. Zhang, B. Qi, Z. Jin, D. Chi, Z. Qi, Y. F. Li and J. Z. Wang, *Energy & Environ. Sci.* **2014**, 7, 1966-1973.

[26] M. Sowinska, S. Brizzi, C. Das, I. Kärkkänen, J. Schneidewind, F. Naumann, H. Gargouri, K. Henkel, D. Schmeißer, *Appl. Surf. Sci.* **2016**, 381, 42-47.

[27] M. Sowinska, K. Henkel, D. Schmeißer, *J. Vac. Sci. Technol. A* **2016**, 34, 01A127

[28] M. Sellers, E. G. Seebauer, *Thin Solid Films* **2011**, 519, 2103-2110.

[29] R. Krol, A. Goossens, J. Schoonman, *J. Electrochem. Soc.* **1997**, 144, 1723-1727.

[30] X. Yang, W. Liu, M. De Bastiani, T. Allen, J. Kang, H. Xu, E. Aydin, L. Xu, Q. Bi, H. Dang, E. AlHabshi, K. Kotsovos, A. AlSaggaf, I.Gereige, Y. Wan, J. Peng, C. Samundsett, A. Cuevas, S. De Wolf, *Joule* **2019**, 3, 1314-1327.

[31] H. C. Card, *IEEE Trans. Electron Devices* **1976**, 23, 538-544.

[32] R. H. Cox, H. Strack, *Solid-State Electron.* **1967**, 10, 1213-1218.

[33] R. Labie, T. Bearda, O. E. Daif, B. O'Sullivan, K. Baert, I. Gordon, *J. Appl. Phys.* **2014**, 115, 183508.

[34] D. Lachenal, P. Papet, B. Legradic, R. Kramer, T. Kössler, L. Andreetta, N. Holm, W. Frammelsberger, D. L. Baetzner, B. Strahm, L. L. Senaud, J. W. Schüttauf, A. Descoeudres, G. Christmann, S. Nicolay, M. Despeisse, B. Paviet-Salomon, C. Ballif, *Sol. Energy Mater. Sol. Cells,* **2019**, 200, 110036.

[35] A. Cuevas, Y. Wan, D. Yan, C. Samundsett, T. Allen, X. Zhang, J. Cui, J. Bullock, *Sol. Energy Mater. Sol. Cells* **2018**, 184, 38-47.

[36] M. A. Green, E. D. Dunlop, J. Hohl-Ebinger, M. Yoshita, N. Kopidakis, A. Ho-Baillie, *Prog. Photovolt. Res. Appl.* **2020**, 28, 3-15.

[37] H. Ali, X. Yang, K. Weber, W. Schoenfeld, K. O. Davis, *Microsc. Microanal.* **2017**, 23, 900-904.

[38] R. Varache, C. Leendertz, M. E. Gueunier-Farret, J. Haschke, D. Munoz, L. Korte, *Sol. Energy Mater. Sol. Cells* **2015**, 141, 14-23.

[39] Z. Liang, Q. Zhang, L. Jiang, G. Cao, *Energy Environ. Sci*. **2015**, 8, 3442-3476.

[40] S. Bi, X. Leng, Y. Li, Z. Zheng, X. Zhang, Y. Zhang, H. Zhou, *Adv. Mater.* **2019**, 31, 1805708.

[41] X. Liu, X. Li, Y. Li, C. Song, L. Zhu, W. Zhang, H. Q. Wang, J. Fang, *Adv. Mater.* **2016**, 28, 7405-7412.

[42] A. Kyaw, X. Sun, C. Jiang, G. Lo, D. W. Zhao, D. L. Kwong, *Appl. Phys. Lett.* **2008**, 93, 221107.

[43] M. S. White, D. C. Olson, S. E. Shaheen, N. Kopidakis, D. S. Ginley, *Appl. Phys. Lett*. **2006**, 89, 143517.

[44] S. K. Hau, H. L. Yip, O. Acton, N. S. Baek, H. Ma, A. Jen, *J. Mater. Chem*. **2008**, 18, 5113-5119

[45] A. Manor, E. A. Katz, T. Tromholt, F. C. Krebs, *Adv. Energy Mater.* **2011**, 1, 836-843.

[46] S. Trost, T. Becker, A. Polywka, P. Görrn, M. F. Oszajca, N. A. Luechinger, D. Rogalla, M. Weidner, P. Reckers, T. Mayer, T. Riedl, *Adv. Energy Mater.* **2016**, 6, 1600347.

[47] P. Schilinsky and C. Waldauf, *Appl. Phys. Lett.* **2002**, 81, 3885.

[48] Y. Lin, B. Adilbekova, Y. Firdaus, E. Yengel, H. Faber, M. Sajjad, X. Zheng, E. Yarali, A. Seitkhan, O. M. Bakr, A. El-Labban, U. Schwingenschlögl, V. Tung, I. McCulloch, F. Laquai, T. D. Anthopoulos, *Adv. Mater.* **2019**, 31, 1902965.